


Structural, Electronic and Thermodynamic Properties of Double Perovskite Cs₂NiF₆: A First-Principles Study

Archana ¹, Preeti Kumari ¹, Navdeep Kaur ¹, Ramesh Sharma ², Vipul Srivastava ^{1,*} 

¹ Department of Physics, School of Chemical Engineering and Physical Sciences, Lovely Professional University, Phagwara-144411, (Punjab) India

² Department of Applied Science, Feroze Gandhi Institute of Engineering and Technology, Raebareli-229001, (Uttar Pradesh) India

* Correspondence: vipsri27@gmail.com;

Scopus Author ID: 16164068800

Received: 29.11.2023; Accepted: 20.12.2023; Published: 17.02.2024

Abstract: The halide perovskite materials are being studied owing to their significant optical and thermoelectric properties and attractive applications in solar cells, LEDs, magnetic, optoelectronic, and temperature-resistive devices. Therefore, the electronic, structural, and thermodynamic properties of Cs₂NiF₆ have been examined utilizing the WIEN2k code's full-potential linearized augmented plane wave (FP-LAPW) approach based on the DFT. Cs₂NiF₆ crystallizes in the cubic structure, space group Fm-3m (225). Its band profile shows a semiconducting nature with a band gap of 1.79 eV. Further, we have estimated thermodynamic parameters such as bulk modulus, Debye temperature, and thermal expansion coefficient in temperatures varying from 0 to 1200K and pressures from 0 to 30 GPa using the QHD model.

Keywords: double perovskites; Wien2k; thermodynamic properties; DFT; Cs₂NiF₆.

© 2024 by the authors. This article is an open-access article distributed under the terms and conditions of the Creative Commons Attribution (CC BY) license (<https://creativecommons.org/licenses/by/4.0/>).

1. Introduction

The perovskite materials having the general formula ABX₃ were first discovered by "Gustav Rose in 1839" [1]. Perovskites are in high demand because of their remarkable applications in solar cells, optoelectronic devices, and thermoelectric devices [2-10]. The notable advancements in the perovskite solar cells can be credited to the exceptional photovoltaic properties exhibited by lead halide perovskites, which include relatively low effective masses for holes and electrons, high optical absorption coefficients, excellent stability, good defect tolerance, large diffusion lengths of photo-generated charge carriers, and tunable direct bandgap energy. In recent years, there has been a significant improvement in the efficiency of perovskite materials, with values increasing from 2.2% to 20.1% [11-15]. However, these compounds contain Pb, which is considered to be toxic and unstable against temperature and moisture. Sn or Ge can replace lead, but these perovskites have a self-doping effect [16], so another possibility is to study double perovskites. Double perovskites have gained interest as alternatives to traditional perovskite solar cells. They offer improved stability and environmental durability compared to their single perovskite counterparts.

The double perovskites, represented by the general formula, A₂BB'X₆, where A is a rare earth element, B and B' are cations, and X can oxide or halides, have applications in the field of industry and technology. The vacancy ordered double perovskite is A₂BX₆, where A, B, and

X represent tetravalent, octavalent cation, and halide, respectively. These halide perovskites can be the replacement of lead halide perovskites. Researchers are studying various vacancy-ordered double perovskites for their applications in optoelectronic devices and other renewable energy technologies [17-31,50-51]. Rb_2ZrCl_6 exhibits impressive resistance to high temperatures, ultraviolet radiation, and exposure to moisture and oxygen in the environment [21]. Recently, Cs-based double perovskites have been prepared experimentally and studied. Wang et al. conducted a study to identify the potential use of double perovskites for optoelectronic applications in the industry [14]. They explored several novel double perovskites and proposed their potential applications in solar cells. In recent studies, several potential materials, such as Cs_2SnI_6 and Cs_2PdBr_6 , have been synthesized based on theoretical predictions [17]. Fang et al. prepared the Cs_2SnI_6 powder and studied the application in solid-state dye-sensitized solar cells and obtained PCE of 6.14% by using an additive in the Cs_2SnI_6 electrolyte [28]. Ali M. et al. investigated Cs_2NiCl_6 and Cs_2NiBr_6 and found them to have extremely narrow bandgaps. These materials are well-suited for optoelectronic applications in visible and ultraviolet light regions due to their ability to exhibit multiple absorption peaks within the energy range of 1 eV [27]. Fernandez et al. studied the XRD pattern of Cs_2TeI_6 powder, which shows the cubic structure (space group Fm-3m) and calculated optical gaps of 1.5eV [29]. However, the exploration of stable halide perovskites without lead and with small band gaps continues to be an active research area. Vacancy-ordered double perovskite can serve as an alternative to lead-based halide perovskite. From the literature survey, we found that the properties of Cs_2NiF_6 have not been calculated till now. Thus, we have performed calculations to determine the electronic, thermodynamic, and structural properties of Cs_2NiF_6 in WIEN2k code based on density functional theory (DFT).

Section 1 contains a brief introduction to the perovskite materials. Section 2 includes computational details used for the present calculations. Section 3 demonstrates the results obtained from the calculations. In the last section, the conclusion is presented.

2. Computational details

Cs_2NiF_6 has been studied for its electronic, thermodynamic, and structural properties utilizing the WIEN2k code's FP-LAPW approach [32-33], which is based on DFT [34]. "Perdew Burke Ernzerhof Generalized Gradient Approximation(PBE-GGA)" and PBEsol ("Perdew-Burke-Ernzerhof solid-state") exchange-correlation potential are used in calculations to describe the electronic structure and properties of the materials [35-36]. The ground state optimization is solved by "Birch Murnaghan equation" [37].

The maximum angular momentum l_{max} was modified to 10, and $R_{\text{MT}} \times K_{\text{max}}$ was set to 7 where R_{MT} and K_{max} defines the size of the muffin-tin sphere and the maximum wave vector allowed in the calculation. The core leakage has been prevented by setting energy and charge convergence to 10^{-3} Ry and 10^{-3} e/a.u.³, respectively. Fourier transformation vector G_{max} was set to 12 a.u.⁻¹. We take R_{MT} values as 2.28, 1.72, and 1.30 a.u for Cs, Ni, and F, respectively. The numbers of K-points are set to be 1000. The mechanical properties of Cs_2NiF_6 are estimated using an IR-elast package in WIEN2k [38].

The thermodynamic parameters of Cs_2NiF_6 were determined using the quasi-harmonic Debye model (QHD) at different temperatures and pressures [39-41]. This model takes into account the thermal vibrations of atoms and provides estimates of thermodynamic properties such as entropy, heat capacity, and free energy as a function of temperature and pressure. The Gibbs function is minimized by optimizing the volume of the system:

$$\left[\frac{\partial G^*}{\partial V} \right]_{p,T} \tag{1}$$

Equation 1 can be solved to obtain the thermal equation of state, which can be utilized to calculate the Debye temperature, thermal expansion coefficient, isothermal bulk modulus, and Gruneisen constant.

3. Results

3.1. Structural properties.

In cubic structure, different atoms of Cs₂NiF₆ occupy different positions: Cs at an atomic position of (0.25, 0.25, 0.25), Ni at (0.5, 0, 0), and F at (0, 0.298161, 0) shown in Figure 1 with space group Fm-3m (225) [42].

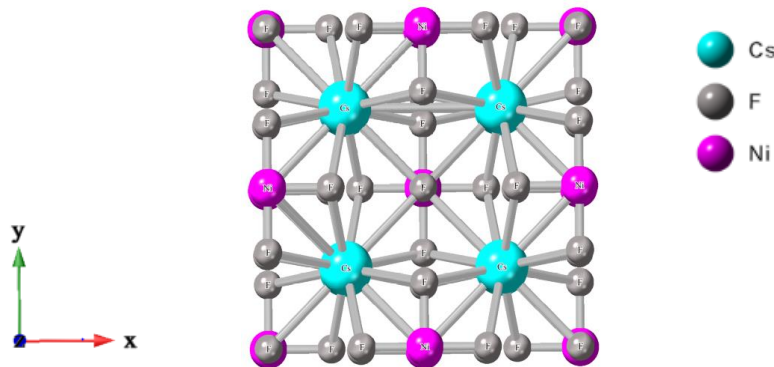


Figure 1. Crystal structure of Cs₂NiF₆

The A₂BX₆ structure comprises six separate [BX₆] octahedra, each providing a 12-fold coordination environment for individual X anions. These [BX₆] octahedra assume a cubic arrangement when positioned at the corners and face center positions. The optimization is done using GGA and PBEsol potentials. The optimized lattice parameter was evaluated by an optimized curve of total energy and volume obtained using "Birch Murnaghan equation of state" (eq 2) as demonstrated in Figure 2.

$$E = E_0 + \frac{9V_0 B_0}{16} \left[\left\{ \left(\frac{V_0}{V} \right)^{\frac{2}{3}} - 1 \right\}^3 B_0 + \left\{ \left(\frac{V_0}{V} \right)^{\frac{2}{3}} - 1 \right\}^2 \left\{ 6 - 4 \left(\frac{V_0}{V} \right)^{\frac{2}{3}} \right\} \right] \tag{2}$$

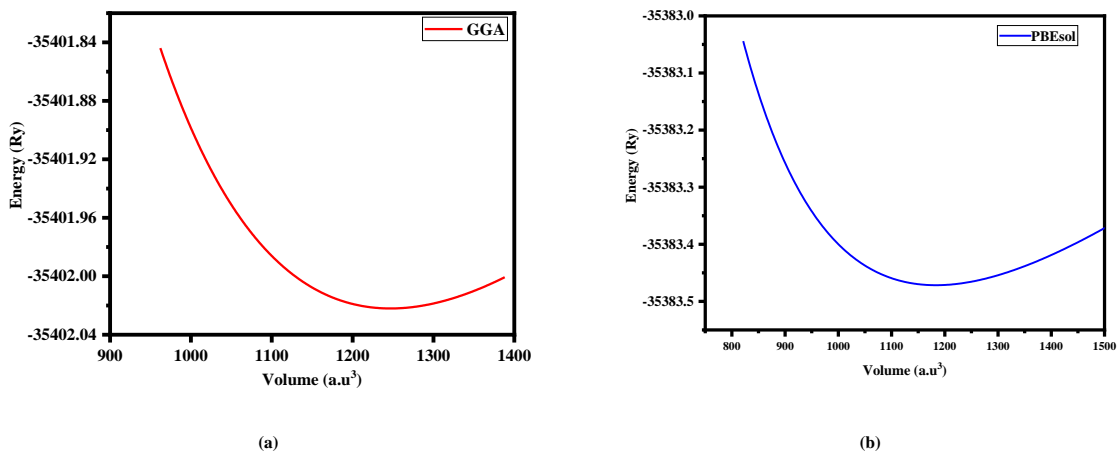


Figure 2. Optimized curve of Cs₂NiF₆ for different exchange potentials **a)** GGA; **b)** PBEsol.

Table 1 presents the determined values of bulk modulus, optimized energy, volume, lattice parameter, and pressure derivative. The optimized lattice parameter (8.88 Å) is found to

be close to the experimental results (8.94 Å) [43]. The PBEsol has the lowest total minimum optimized energy than GGA potential.

The formation energy of Cs₂NiF₆ is calculated using eq 3

$$\Delta H_f = E_{Cs_2NiF_6}^{total} - [2E_{Cs}^{bulk} + E_{Ni}^{bulk} + 6E_F^{bulk}] \quad (3)$$

where E_{Cs}^{bulk} , E_{Ni}^{bulk} , E_F^{bulk} are the energies of the fundamental state per atom of Cs, Ni, F, and $E_{Cs_2NiF_6}^{total}$ gives the total energy of Cs₂NiF₆. The formation energy is calculated to be -2.43eV/atom. The studied material is stable owing to its negative formation energy.

Also we have calculated the cohesive energy of Cs₂NiF₆ using the equation 4.

$$E_{coh} = 2E_{Cs}^{iso} + E_{Ni}^{iso} + 6E_F^{iso} - E_{Cs_2NiF_6}^{total} \quad (4)$$

where E_{Cs}^{iso} , E_{Ni}^{iso} and E_F^{iso} denote total energies of isolated atoms and $E_{Cs_2NiF_6}^{total}$ is the total ground state energy of Cs₂NiF₆. The value of cohesive energy is found to be 4.01 eV/atom which indicates that the material is stable.

Table 1. Ground state values of lattice parameter, volume, E₀, B, and B'.

Parameters	Present study		Experimental/others
	GGA	PBEsol	
Lattice constant, a (Å)	9.04	8.88	8.94 [43] 8.81 [14]
Volume, V (a.u. ³)	1246.3304	1181.5678	-
E ₀ (Ry)	-35402.022	-35383.471	-
Bulk modulus, B (GPa)	47.73	54.59	-
Pressure derivative, B'	5.07	4.99	-

3.2. Electronic properties.

Figure 3 depicts the electronic band structure of Cs₂NiF₆. The band gap of Cs₂NiF₆ is calculated to be 1.795 eV, with the conduction band (CB) minima located at the X point in the Brillouin zone, while the valence band (VB) maxima are situated at the Γ point. This indicates that Cs₂NiF₆ has an indirect band gap and semiconducting nature. Cs₂NiF₆ has a small band gap, which can be useful in optoelectronic applications [29].

The density of states (DOS) was employed to analyze and gain insights into the electronic properties of Cs₂NiF₆. Figure 4 displays the total DOS plots, which suggest that the material is semiconducting. Understanding the orbital properties aids in elucidating the electronic contributions of individual atoms to the stabilized structure. The Positioning of Cs orbitals significantly away from the Fermi level indicates that Cs has minimal influence on the band edge states in Cs₂NiF₆. Furthermore, both the Ni and F orbitals play a role in forming the CB edge and VB edge.

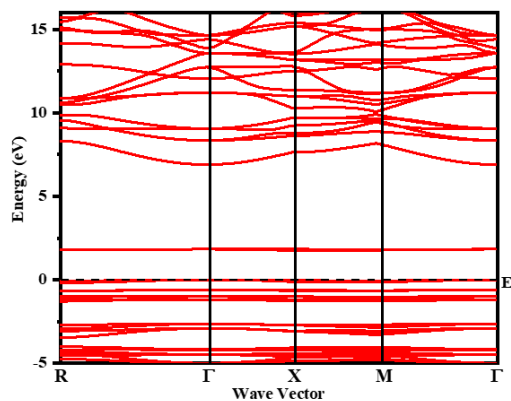


Figure 3. Band structure of halide double perovskite Cs₂NiF₆.

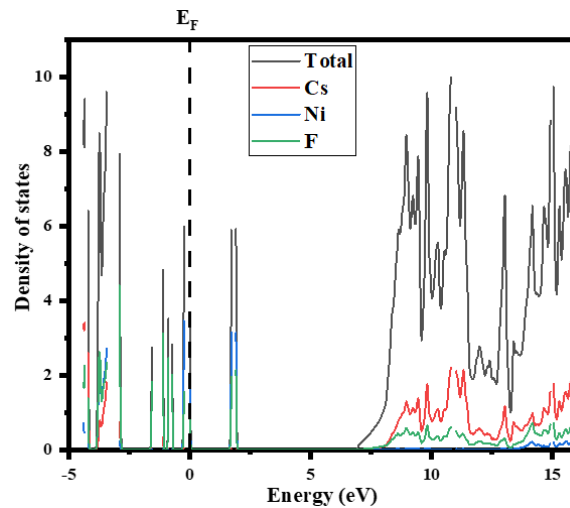


Figure 4. Total density of state plot of Cs₂NiF₆.

3.3. Elastic and mechanical properties.

Alternatively, the stability of materials under compression is determined by the elastic constants. Therefore, the mechanical properties of Cs₂NiF₆ are estimated using the IR-elast package in WIEN2k [38] code. These constants also tell about the bonding nature, ductile/brittle nature, and melting temperature. Cs₂NiF₆ has a cubic structure, which is also satisfied by the criteria

$$C_{11} > 0, C_{44} > 0, C_{11} - C_{12} > 0, C_{11} + 2C_{12} > 0 \quad (5)$$

The values of elastic constants are predicted to be 77.44 GPa, 6.71 GPa, and 17.38 GPa for C₁₁, C₁₂, and C₄₄, respectively. The estimated values satisfy the criteria of stable cubic structure given by Eq 4. The Voigt-Reuss-Hill approximation [44-46] is used to calculate properties like bulk modulus and shear modulus by using eq (6-10)

Bulk modulus:

$$B = \frac{1}{3}(C_{11} + 2C_{12}) \quad (6)$$

Voigt's shear modulus

$$G_V = \frac{1}{5}(C_{11} - C_{12} + 3C_{44}) \quad (7)$$

Reuss's shear modulus:

$$G_R = \frac{5(C_{11} - C_{12})C_{44}}{3(C_{11} - C_{12}) + C_{44}} \quad (8)$$

Shear modulus:

$$G = \frac{1}{2}(G_V + G_R) \quad (9)$$

Young's modulus:

$$Y = \frac{9BG}{3B + G} \quad (10)$$

The calculated values are given in Table 2. The ratio of bulk modulus to the Shear modulus (B/G) explains the nature of materials [47]. Cs₂NiF₆ shows a brittle nature as the value of B/G is 1.3. This is also verified by the negative value of Cauchy's pressure factor, C₁₂ - C₄₄ (-10.66 GPa) [48].

Table 2. Calculated elastic constants C_{11} , C_{12} , C_{44} in (GPa), B (GPa), Voigt shear modulus G_V (GPa), Reuss shear modulus G_R (GPa), shear modulus G (GPa), Young's modulus Y (GPa), Cauchy pressure ($C_{12}-C_{44}$) (GPa), Poisson's ratio ν , B/G ratio and melting temperature T_m (K) for Cs_2NiF_6 .

Properties	Cs_2NiF_6
C_{11}	77.44
C_{12}	6.71
C_{44}	17.38
B	30.29
G_V	24.57
G_R	21.82
G	23.19
Y	55.44
$C_{12}-C_{44}$	-10.66
ν	0.19
B/G	1.30
T_m	1010 ± 300 K

The bonding nature is predicted by the Poisson ratio, which is given by:

$$\nu = \frac{3B-2G}{2(3B+G)} \quad (11)$$

Materials have covalent bonding if $\nu = 0.1$, ionic if $\nu = 0.25$ and metallic if $\nu = 0.33$ [48]. The Poisson ratio is calculated to be 0.19 for Cs_2NiF_6 , indicating covalent bonding. The melting temperature has been theoretically calculated using Eq 12 [49].

$$T_m = [(553 + 5.911 C_{11}) \pm 300 K] \quad (12)$$

The value of T_m is found to be 1010 ± 300 K.

3.4. Thermodynamic properties.

Thermodynamic parameters were calculated using the QHD model for Cs_2NiF_6 at various temperatures and pressures to assess the applicability of Cs_2NiF_6 in various industry applications. For calculating thermal parameters, the Gibbs function (G^*) should be kept to a minimum in terms of volume at constant pressure and temperature [39-41].

$$\left[\frac{\partial G^*}{\partial V} \right]_{p,T} = 0 \quad (13)$$

Debye temperature (θ_D), Grüneisen parameter (γ), Bulk modulus (B), and thermal expansion coefficient (α), were calculated by using Equations (14-17).

$$B = \left[V \left(\frac{\partial^2 G^*}{\partial V^2} \right)_{p,T} \right]_{v_{opt}(p,T)} \quad (14)$$

$$\gamma = - \frac{d \ln \theta_D}{d \ln V} \quad (15)$$

$$\alpha = \frac{1}{V} \left[\frac{\partial V}{\partial T} \right]_p \quad (16)$$

$$\theta_D = \frac{h}{k} \left[6\pi^2 V^{\frac{1}{3}} n \right]^{\frac{1}{3}} f(\nu) \sqrt{\frac{B_s}{M}} \quad (17)$$

ν is Poisson's ratio, B_s is the adiabatic bulk modulus. The estimated thermodynamic parameters values at $T=0, 300K$ and at $P=0$ GPa is shown in Table 3.

Table 3. Thermodynamic parameters at $P=0$ GPa, $T=0,300K$.

Thermodynamic parameter	Temperature	
	$T=0K$	$T=300K$
Bulk modulus, B (GPa)	54.50	51.83
Thermal expansion Coefficient, α (K^{-1})	0	3.19×10^{-5}

Thermodynamic parameter	Temperature	
Debye Temperature, θ_D (K)	50.67	49.64
Grüneisen parameter, γ	2.33	2.35

The behavior of the bulk modulus (B) under pressure and temperature was analyzed for the material under investigation. By studying the variation of B with different temperatures and pressures, insights were gained into how the material's mechanical properties respond to these external conditions. In Figure 5, a variation of bulk modulus with temperature (0K-1200K) for various pressure values from 0GPa to 30GPa is presented. It is noted that with increasing temperature B decreases, while with increased pressure, bulk modulus increases. It indicates that the hardness of a material is reduced by increasing temperature. The behavior of bulk modulus under temperature and pressure is a fairly common trend where an increase in temperature results in reduced hardness [50].

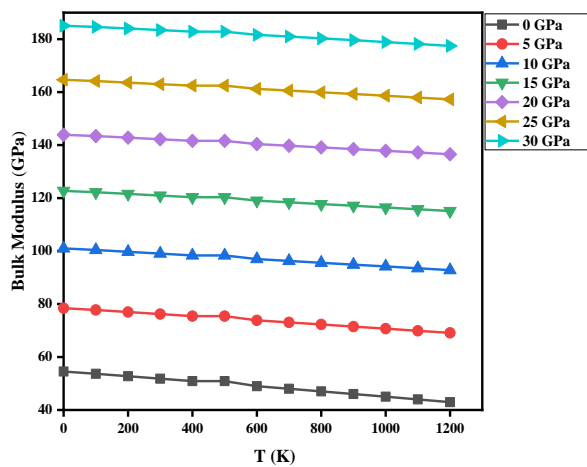


Figure 5. Change in B with pressure and temperature.

The expansion and contraction of the solids can be determined by the thermal expansion coefficient. The solids contract when pressure is increased, while it expands when temperature is increased. Figure 6 shows the change in the thermal expansion coefficient. It increases sharply at 100 K, and after that, it increases slowly, whereas as the pressure rises, its value decreases, which is similar to behavior in other perovskites [6]. The estimated value of α at 300K and 0 GPa is found to be $3.19 \times 10^{-5} \text{ K}^{-1}$.

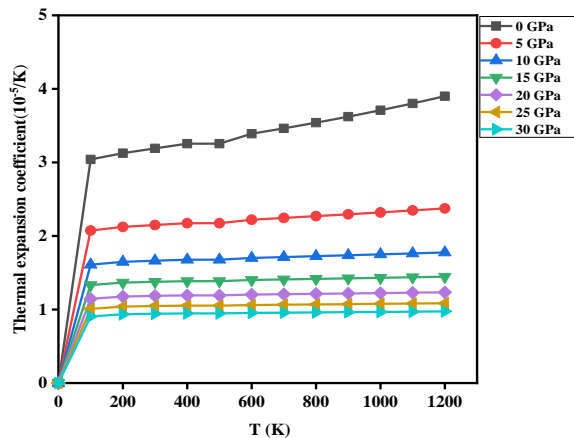


Figure 6. Change in α with temperature and pressure.

Debye temperature (θ_D) denotes the peak temperature as a result of a single mode of vibrations [3]. Figure 7 presents the change in θ_D with changes in temperature (0-1200 K) and <https://biointerfaceresearch.com/>

pressure (0-30 GPa). It is observed that θ_D reduces slowly as the temperature rises from 0 K to 1200K whereas θ_D increases as pressure increases. The value of θ_D is estimated to be 50.67 K at 0 K and 0 GPa.

Grüneisen parameter (γ) tells us about the degree of anharmonicity of the solids [51]. In Figure 8, a change in γ with temperature and pressure is presented. Grüneisen parameter increases slowly with an increase in temperature, but it reduces rapidly with a rise in pressure. This indicates that anharmonicity decreases in Cs_2NiF_6 with the rise in pressure. The value of γ is 2.35 at 0 GPa, which reduces to 1.86 at 30 GPa and 300K.

The properties of Cs_2NiF_6 have not been investigated other than its structural properties. The lattice constant obtained from the optimized curve is in agreement with the experimental value and other work, whereas other parameters are calculated for the first time, and they are similar to another kind of double perovskite materials [2,3,6,30,31].

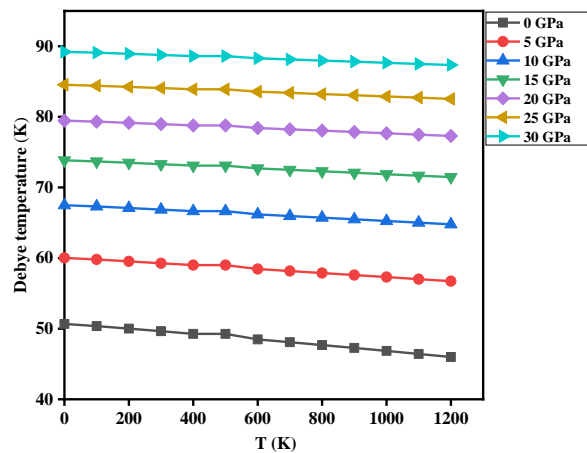


Figure 7. Change in θ_D with temperature and pressure.

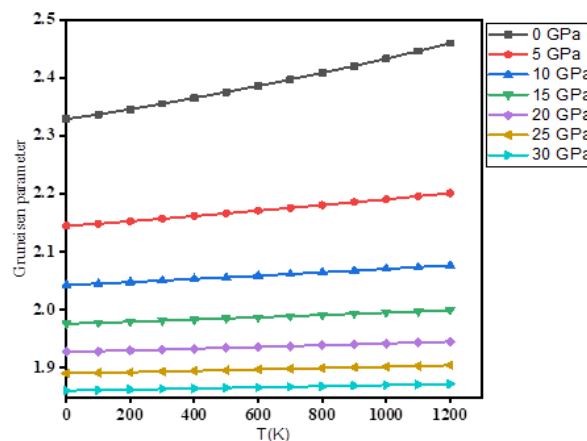


Figure 8. Change in γ with temperature and pressure.

4. Conclusions

The structural, thermodynamic, and electrical properties of Cs_2NiF_6 have all been examined and analyzed in the WIEN2k code using DFT. Its structure is stable in cubical form, having an Fm-3m (225) space group. Cs_2NiF_6 shows an indirect band gap of 1.795 eV and a semiconducting nature. Thermodynamic parameters are obtained using QHD model. The hardness of the material is reduced by increasing temperature, and anharmonicity decreases in Cs_2NiF_6 with a rise in pressure. The value of α , θ_D and γ were estimated to be $3.19 \times 10^{-5}\text{K}^{-1}$, 49.64 K, and 2.35, respectively at 300 K.

Funding

This research received no external funding.

Acknowledgments

Presented in 4th International Conference on "Recent Advances in Fundamental and Applied Sciences" (RAFAS-2023)" on March 24-25, 2023, Organized by the School of Chemical Engineering and Physical Sciences, Lovely Professional University, Punjab, India.

Conflict of Interests

The authors declare that there is no conflict of interest.

References

1. Bhalla, A.S.; Guo, R.; Roy, R. The perovskite structure—a review of its role in ceramic science and technology. *Mater. Res. Innov.* **2000**, *4*, 3-26, <https://doi.org/10.1007/s100190000062>.
2. Kumari, P.; Sharma, R.; Lilhore, U.; Khenata, R.; Srivastava, V. First-principles study on structural, electronic, elastic, mechanical, thermodynamic, and thermoelectric properties of RbSnX_3 (X= F, Cl, and Br) perovskites. *Int. J. Energy Res.* **2022**, *46*, 23893-23907, <https://doi.org/10.1002/er.8687>.
3. Kumari, P.; Sharma, R.; Al-Douri, Y.; Srivastava, V. Electronic, thermodynamical and thermoelectric performances of RbSnI_3 halide perovskite for photovoltaic cell and UV absorber applications. *Mater. Today Commun.* **2023**, *36*, 106752, <https://doi.org/10.1016/j.mtcomm.2023.106752>.
4. Chen, Y.; Zhang, L.; Zhang, Y.; Gao, H.; Yan, H. Large-area perovskite solar cells—a review of recent progress and issues. *RSC Adv.* **2018**, *8*, 10489-10508, <https://doi.org/10.1039/C8RA00384J>.
5. Park, N.-G. Perovskite solar cells: an emerging photovoltaic technology. *Mater. Today* **2015**, *18*, 65-72, <https://doi.org/10.1016/j.mattod.2014.07.007>.
6. Kumari, P.; Srivastava, V.; Khenata, R.; Dar, S.A.; Naqib, S.H. A first-principles prediction of thermophysical and thermoelectric performances of SrCeO_3 perovskite. *Int. J. Energy Res.* **2022**, *46*, 2934-2946, <https://doi.org/10.1002/er.7354>.
7. Huang, H.; Polavarapu, L.; Sichert, J.A.; Susha, A.S.; Urban, A.S.; Rogach, A.L. Colloidal lead halide perovskite nanocrystals: synthesis, optical properties and applications. *NPG Asia Mater.* **2016**, *8*, e328, <https://doi.org/10.1038/am.2016.167>.
8. Sharma, R.; Dey, A.; Dar, S.A.; Srivastava, V. A DFT investigation of CsMgX_3 (X= Cl, Br) halide perovskites: Electronic, thermoelectric and optical properties. *Comput. Theor. Chem.* **2021**, *1204*, 113415, <https://doi.org/10.1016/j.comptc.2021.113415>.
9. Kim, H.-S.; Lee, C.-R.; Im, J.-H.; Lee, K.-B.; Moehl, T.; Marchioro, A.; Moon, S.-J.; Humphry-Baker, R.; Yum, J.-H.; Moser, J.E.; Grätzel, M.; Park, N.-G. Lead Iodide Perovskite Sensitized All-Solid-State Submicron Thin Film Mesoscopic Solar Cell with Efficiency Exceeding 9%. *Sci. Rep.* **2012**, *2*, 591, <https://doi.org/10.1038/srep00591>.
10. Lee, M.M.; Teuscher, J.; Miyasaka, T.; Murakami, T.N.; Snaith, H.J. Efficient Hybrid Solar Cells Based on Meso-Superstructured Organometal Halide Perovskites. *Science* **2012**, *338*, 643-647, <https://doi.org/10.1126/science.1228604>.
11. Sharma, R.; Dar, S.A.; Albalawi, H.; Alqahtani, M.S.; Srivastava, V. Modeling of structural, electronic, optical, and thermoelectric properties of $\text{CsPb}(\text{I}_{1-x}\text{Br}_x)_3$ (x= 0, 1, 2, 3) solid solutions by first principle approach. *Chin. J. Phys.* **2023**, *85*, 264-276, <https://doi.org/10.1016/j.cjph.2023.07.013>.
12. Swarnkar, A.; Marshall, A.R.; Sanehira, E.M.; Chernomordik, B.D.; Moore, D.T.; Christians, J.A.; Chakrabarti, T.; Luther, J.M. Quantum dot-induced phase stabilization of α - CsPbI_3 perovskite for high-efficiency photovoltaics. *Science* **2016**, *354*, 92-95, <https://doi.org/10.1126/science.aag2700>.
13. Jeong, J.; Kim, M.; Seo, J.; Lu, H.; Ahlawat, P.; Mishra, A.; Yang, Y.; Hope, M.A.; Eickemeyer, F.T.; Kim, M.; Yoon, Y.J.; Choi, I.W.; Darwich, B.P.; Choi, S.J.; Jo, Y.; Lee, J.H.; Walker, B.; Zakeeruddin, S.M.; Emsley, L.; Rothlisberger, U.; Hagfeldt, A.; Kim, D.S.; Grätzel, M.; Kim, J.Y. Pseudo-halide anion engineering for α - FAPbI_3 perovskite solar cells. *Nature* **2021**, *592*, 381-385, <https://doi.org/10.1038/s41586-021-03406-5>.

14. Brik, M.G.; Kityk, I.V. Modeling of lattice constant and their relations with ionic radii and electronegativity of constituting ions of A_2XY_6 cubic crystals (A= K, Cs, Rb, Tl; X= tetravalent cation, Y= F, Cl, Br, I). *J. Phys. Chem. Solids* **2011**, *72*, 1256-1260, <https://doi.org/10.1016/j.jpcs.2011.07.016>.
15. Manser, J.S.; Christians, J.A.; Kamat, P.V. Intriguing Optoelectronic Properties of Metal Halide Perovskites. *Chem. Rev.* **2016**, *116*, 12956-13008, <https://doi.org/10.1021/acs.chemrev.6b00136>.
16. Kour, R.; Arya, S.; Verma, S.; Gupta, J.; Bandhoria, P.; Bharti, V.; Datt, R.; Gupta, V. Potential Substitutes for Replacement of Lead in Perovskite Solar Cells: A Review. *Global Chall.* **2019**, *3*, 1900050, <https://doi.org/10.1002/gch2.201900050>.
17. Ray, A.; De Trizio, L.; Zito, J.; Infante, I.; Manna, L.; Abdelhady, A.L. Light Emission from Low-Dimensional Pb-Free Perovskite-Related Metal Halide Nanocrystals. *Adv. Opt. Mater.* **2023**, *11*, 2202005, <https://doi.org/10.1002/adom.202202005>.
18. Nassah, Y.; Benmakhlof, A.; Hadjeris, L.; Helaimia, T.; Khenata, R.; Bouhemadou, A.; Omran Bin, S.; Sharma, R.; Said, G.S.; Srivastava, V. Electronic band structure, mechanical and optical characteristics of new lead-free halide perovskites for solar cell applications based on DFT computation. *Bull. Mater. Sci.* **2023**, *46*, 55, <https://doi.org/10.1007/s12034-023-02890-x>.
19. Talebi, M.; Mokhtari, A.; Soleimanian, V. Ab-initio simulation of the structural, electronic and optical properties for the vacancy-ordered double perovskites A_2TiI_6 (A= Cs or NH_4); a time-dependent density functional theory study. *J. Phys. Chem. Solids* **2023**, *176*, 111262, <https://doi.org/10.1016/j.jpcs.2023.111262>.
20. Berri, S. Thermoelectric properties of A_2BCl_6 : A first principles study. *J. Phys. Chem. Solids* **2022**, *170*, 110940, <https://doi.org/10.1016/j.jpcs.2022.110940>.
21. Zhang, F.; Chen, Z.; Liu, Z.; Jia, M.; Chen, X.; Wu, D.; Li, X.; Shi, Z. Highly stable vacancy-ordered double perovskite Rb_2ZrCl_6 with broadband emission for down-conversion white light-emitting diodes. *J. Lumin.* **2022**, *251*, 119150, <https://doi.org/10.1016/j.jlumin.2022.119150>.
22. Ye, X.; Liu, A.; Gao, L.; Zhang, C.; Yan, L.; Wen, S.; Ma, T. Computational screening of Cs based vacancy-ordered double perovskites for solar cell and photocatalysis applications. *EcoMat* **2023**, *5*, e12295, <https://doi.org/10.1002/eom2.12295>.
23. Al-Muhimeed, T.I.; Aljameel, A.I.; Mera, A.; Saad, S.; Nazir, G.; Albalawi, H.; Bouzgarrou, S.; Hegazy, H.H.; Mahmood, Q. First principle study of optoelectronic and mechanical properties of lead-free double perovskites Cs_2SeX_6 (X= Cl, Br, I). *J. Taibah Univ. Sci.* **2022**, *16*, 155-162, <https://doi.org/10.1080/16583655.2022.2035927>.
24. Mahmood, Q.; Hassan, M.; Yousaf, N.; AlObaid, A.A.; Al-Muhimeed, T.I.; Morsi, M.; Albalawi, H.; Alamri, O.A. Study of lead-free double perovskites halides Cs_2TiCl_6 , and Cs_2TiBr_6 for optoelectronics, and thermoelectric applications. *Mater. Sci. Semicond. Process.* **2022**, *137*, 106180, <https://doi.org/10.1016/j.mssp.2021.106180>.
25. Noman, M.; Neffati, R.; Khan, S.; Murad, K.; Ashraf, M.W.; Murtaza, G. The halide ion replacement effects on the physical properties of Cs_2BX_6 variant perovskites. *Phys. B: Condens. Matter* **2023**, *656*, 414779, <https://doi.org/10.1016/j.physb.2023.414779>.
26. Ye, X.; Liu, A.; Zhao, Y.; Han, Q.; Kitamura, T.; Ma, T. DFT study of X-site ion substitution doping of Cs_2PtX_6 on its structural and electronic properties. *Int. J. Energy Res.* **2022**, *46*, 8471-8479, <https://doi.org/10.1002/er.7696>.
27. Ali, M.; Haldera, P.; Hossain, M.; Biswas, J.P.; Sarker, S.; Kamruzzaman; Nurujjaman, N.; Thamid, T.; Ali, I.; Chakma, U.; Kumer, A. A study on pseudo-potential effect, electronic structure, aquatic toxicity, and optical properties of perovskites solar cell of Cs_2NiCl_6 , Cs_2NiBr_6 , and Cs_2PtBr_6 : Through DFT methods. *Curr. Chem. Lett.* **2023**, *12*, 557-566, <http://doi.org/10.5267/j.ccl.2023.2.007>.
28. Fang D.; Tan, Y.; Ren Y.; Zheng S.; Xiong, F.; Wang, A.; Chang, K.; Mi, B.; Cao, D.; Gao, Z. Simple Solution Preparation of Cs_2SnI_6 Films and Their Applications in Solid-State DSSCs. *ACS Appl. Mater. Interfaces* **2023**, *15*, 32538-32551, <https://doi.org/10.1021/acsami.3c04807>.
29. Vázquez-Fernández, I.; Mariotti, S.; Hutter, O.S.; Birkett, M.; Veal, T.D.; Hobson, T.D.C.; Phillips, L.J.; Danos, L.; Nayak, P.K.; Snaith, H.J.; Xie, W.; Sherburne, M.P.; Asta, M.; Durose, K. Vacancy-Ordered Double Perovskite Cs_2TeI_6 Thin Films for Optoelectronics. *Chem. Mater.* **2020**, *32*, 6676-6684, <https://doi.org/10.1021/acs.chemmater.0c02150>.
30. Kumari, P.; Sharma, R.; Srivastava, V.; Khenata, R. Abinitio calculations of structural, electronic, and thermodynamic performance of Cs_2GeF_6 perovskite. *AIP Conf. Proc.* **2023**, *2800*, 020010, <https://doi.org/10.1063/5.0163083>.

31. Kumari, P.; Ashwathkumaran, C.; Srivastava, V. DFT calculations on heat capacity and Debye temperature of Cs₂GeF₆ perovskite under high temperature and pressure. *AIP Conf. Proc.* **2023**, *2800*, 020315, <https://doi.org/10.1063/5.0163161>.
32. Blaha, P.; Schwarz, K.; Sorantin, P.; Trickey, S.B. Full-potential, linearized augmented plane wave programs for crystalline systems. *Comput. Phys. Commun.* **1990**, *59*, 399-415, [https://doi.org/10.1016/0010-4655\(90\)90187-6](https://doi.org/10.1016/0010-4655(90)90187-6).
33. Hohenberg, P.; Kohn, W. Inhomogeneous Electron Gas. *Phys. Rev.* **1964**, *136*, B864, <https://doi.org/10.1103/PhysRev.136.B864>.
34. Blaha, P.; Schwarz, K.; Madsen, G.K.H.; Kvasnicka, D.; Luitz, J. WIEN2k: An Augmented Plane Wave plus Local Orbitals Program for Calculating Crystal Properties. **2001**.
35. Perdew, J.P.; Burke, K.; Ernzerhof, M. Generalized Gradient Approximation Made Simple. *Phys. Rev. Lett.* **1996**, *77*, 3865, <https://doi.org/10.1103/PhysRevLett.77.3865>.
36. Perdew, J.P.; Ruzsinszky, A.; Csonka, G.I.; Vydrov, O.A.; Scuseria, G.E.; Constantin, L.A.; Zhou, X.; Burke, K. Restoring the Density-Gradient Expansion for Exchange in Solids and Surfaces. *Phys. Rev. Lett.* **2008**, *100*, 136406, <https://doi.org/10.1103/PhysRevLett.100.136406>.
37. Birch, F. The Effect of Pressure Upon the Elastic Parameters of Isotropic Solids, According to Murnaghan's Theory of Finite Strain. *J. Appl. Phys.* **1938**, *9*, 279-288, <https://doi.org/10.1063/1.1710417>.
38. Jamal, M.; Bilal, M.; Ahmad, I.; Jalali-Asadabadi, S. IRelast package. *J. Alloys Compd.* **2018**, *735*, 569-579, <https://doi.org/10.1016/j.jallcom.2017.10.139>.
39. Blanco, M.A.; Francisco, E.; Luana, V. GIBBS: isothermal-isobaric thermodynamics of solids from energy curves using a quasi-harmonic Debye model. *Comput. Phys. Commun.* **2004**, *158*, 57-72, <https://doi.org/10.1016/j.comphy.2003.12.001>.
40. Otero-de-la-Roza, A.; Abbasi-Pérez, D.; Luaña, V. G_{IBBS}2: A new version of the quasi-harmonic model code. II. Models for solid-state thermodynamics, features and implementation. *Comput. Phys. Commun.* **2011**, *182*, 2232-2248, <https://doi.org/10.1016/j.cpc.2011.05.009>.
41. Otero-de-la-Roza, A.; Luaña, V. GIBBS2: A new version of the quasi-harmonic model code. I. Robust treatment of the static data. *Comput. Phys. Commun.* **2011**, *182*, 1708-1720, <https://doi.org/10.1016/j.cpc.2011.04.016>.
42. Data retrieved from the Materials Project for Cs₂NiF₆ (mp-689925) from database version v2022.10.28., 02 February 2023, <https://doi.org/10.17188/1284446>.
43. Bode, H.; Voss, E. Über Strukturen von Fluorokomplexen mit vierwertigem Nickel und Chrom. *Z. Anorg. Allg. Chem.* **1956**, *286*, 136-141, <https://doi.org/10.1002/zaac.19562860304>.
44. Hill, R. The Elastic Behaviour of a Crystalline Aggregate. *Proc. Phys. Soc. A* **1952**, *65*, 349, <https://doi.org/10.1088/0370-1298/65/5/307>.
45. Voigt, W. Lehrbuch der Kristallphysik. Teubner Verlag, Leipzig, **1928**.
46. Reuss, A. Berechnung der Fließgrenze von Mischkristallen auf Grund der Plastizitätsbedingung für Einkristalle. *Z. Angew. Math. Mech.* **1929**, *9*, 49-58, <https://doi.org/10.1002/zamm.19290090104>.
47. Pugh, S.F. XCII. Relations between the elastic moduli and the plastic properties of polycrystalline pure metals. *Lond. Edinb. Dublin Philos. Mag. J. Sci.* **1954**, *45*, 823-843, <https://doi.org/10.1080/14786440808520496>.
48. Srivastava, V.; Kaur, N.; Wang, X.; Mushtaq, M.; Dar, S.A. First-principles study on structural, electronic, magnetic, elastic, mechanical and thermodynamic properties of Mn₂PtCo Heusler alloy. *Int. J. Energy Res.* **2021**, *45*, 11305-11319, <https://doi.org/10.1002/er.6559>.
49. Fine, M.E.; Brown, L.D.; Marcus, H.L. Elastic constants versus melting temperature in metals. *Scr. Metallurgica*, **1984**, *18*, 951-956, [https://doi.org/10.1016/0036-9748\(84\)90267-9](https://doi.org/10.1016/0036-9748(84)90267-9).
50. Ali, M.A.; Ullah, R.; Dar, S.A.; Murtaza, G.; Khan, A.; Mahmood, A. Modeling of structural, elastic, mechanical, acoustical, electronic and thermodynamic properties of XPdF₃ (X= Rb, Tl) perovskites through density functional theory. *Phys. Scr.* **2020**, *95*, 075705, <https://doi.org/10.1088/1402-4896/ab8eee>.
51. Porter, L.J.; Justo, J.F.; Yip, S. The importance of Grüneisen parameters in developing interatomic potentials. *J. Appl. Phys.* **1997**, *82*, 5378-5381, <https://doi.org/10.1063/1.366305>.